ARMY RESEARCH LABORATORY

ARL

A Fully Integrated Materials Framework for Enabling the Wireless Detection of Micro-defects in Aging and Battle-worn Structures (Final Report)

by R. C. Toonen, S. G. Hirsch, R. X. Fu, M. P. Ivill, and M. W. Cole

NOTICES

Disclaimers

The findings in this report are not to be construed as an official Department of the Army position unless so designated by other authorized documents.

Citation of manufacturer's or trade names does not constitute an official endorsement or approval of the use thereof.

Destroy this report when it is no longer needed. Do not return it to the originator.

Army Research Laboratory

Aberdeen Proving Ground, MD 21005

ARL-MR-0822 **May 2012**

A Fully Integrated Materials Framework for Enabling the Wireless Detection of Micro-defects in Aging and Battle-worn Structures (Final Report)

R. C. Toonen, S. G. Hirsch, R. X. Fu, M. P. Ivill, and M. W. Cole
Weapons and Materials Research Directorate, ARL

REPORT DOCUMENTATION PAGE

1. REPORT DATE *(DD-MM-YYYY)*	2. REPORT TYPE	3. DATES COVERED (From - To)
May 2012	DRI	

4. TITLE AND SUBTITLE	5a. CONTRACT NUMBER
A Fully Integrated Materials Framework for Enabling the Wireless Detection of Micro-defects in Aging and Battle-worn Structures (Final Report)	
	5b. GRANT NUMBER
	5c. PROGRAM ELEMENT NUMBER

6. AUTHOR(S)	5d. PROJECT NUMBER
R. C. Toonen, S. G. Hirsch, R. X. Fu, M. P. Ivill, and M. W. Cole	
	5e. TASK NUMBER
	5f. WORK UNIT NUMBER

7. PERFORMING ORGANIZATION NAME(S) AND ADDRESS(ES)	8. PERFORMING ORGANIZATION REPORT NUMBER
U.S. Army Research Laboratory ATTN: RDRL-WMM-E Aberdeen Proving Ground, MD 21005	ARL-MR-0822

9. SPONSORING/MONITORING AGENCY NAME(S) AND ADDRESS(ES)	10. SPONSOR/MONITOR'S ACRONYM(S)
	11. SPONSOR/MONITOR'S REPORT NUMBER(S)

12. DISTRIBUTION/AVAILABILITY STATEMENT

Approved for public release; distribution unlimited.

13. SUPPLEMENTARY NOTES

14. ABSTRACT

We present second-year results from a two-year study on a novel, inexpensive, passive, wireless solution for performing nondestructive evaluation on the structural integrity of aging aircraft. Electro-mechanical resonant phenomena in barium strontium titanate thin films have been thoroughly investigated using microwave reflectivity spectroscopy. Additionally, piezoelectric lead zirconate titanate thin films have been electrically characterized in terms of capacitance and dielectric loss tangent. Finally, we have explored the integration of such devices into a detection system involving piezoelectric wafer active transducers.

15. SUBJECT TERMS

barium strontium titanate, lead zirconate titanate, microwave dielectric spectroscopy, third-order nonlinear susceptibility

16. SECURITY CLASSIFICATION OF:			17. LIMITATION OF ABSTRACT	18. NUMBER OF PAGES	19a. NAME OF RESPONSIBLE PERSON R. C. Toonen
a. REPORT	b. ABSTRACT	c. THIS PAGE	UU	34	19b. TELEPHONE NUMBER *(Include area code)* (410) 306-4536
Unclassified	Unclassified	Unclassified			

Contents

Lists of Figures

Acknowledgments

1. Objective

The objective of this body of work is to explore, develop, and demonstrate the feasibility of providing the U.S. Army with inexpensive, scalable, passive, and ultra-low power consuming fully integrated circuits that enable analog information from a piezoelectric sensor to be telemetrically monitored via a radio frequency identification (RFID)-like backscatter transponder. First-year technical progress from a two-year U.S. Army Research Laboratory (ARL) Director's Research Initiative (DRI) sponsored project entitled, "A Fully Integrated Materials Framework for Enabling the Wireless Detection of Micro-Defects in Aging and Battle-Worn Structures" was reported in ARL Memorandum Report, ARL-MR-0775 (*1*). The first-year results presented in that report include reflection phase shifter design and optimization; initial growth studies and characterizations of barium strontium titanate (BST) and lead zirconate titanate (PZT) thin films; thin-film nickel chromium alloy (NiCr) resistor fabrication and testing; and progress towards realizing plated, laser-drilled, through-wafer microvias in sapphire substrates.

In this report, we present technical results from the second-year study, which primarily focused on characterizing and understanding of the physical properties of the BST and PZT thin films. Using microwave reflection spectroscopy, the complex permittivities of etch defined, 240-nm-thick, $(Ba_{0.6}Sr_{0.4})TiO_3$ thin films were measured over the frequency range of (1 to 4) GHz. Anomalous electric-field-induced electro-acoustic resonances were observed and characterized as a function of extrinsic electric field magnitude, ambient temperature, and sample diameter. The real and imaginary parts of the measured permittivities were fit to frequency-dependent functions derived from the Lorentz oscillator model. From these functions, extracted static dielectric constants were found to display excellent agreement with a closed-form expression derived by calculating third-order nonlinear susceptibility from the Landau-Devonshire-Ginzberg model. Finally, the electrical properties of sputtered $Pb_{1+y}[Zr_xTi_{1-x}]O_{3+y}$ (PZT) thin films were studied in terms of frequency- and voltage-dependent capacitance and dielectric loss tangent measurements. Preliminary experiments related to defect detection in aircraft-grade aluminum (Al) panels were demonstrated using both thin-film and bulk PZT.

2. Approach

There is a critical military need to develop the technology of fully integrated, passive telemetric readout systems. Remote sensors accessed via microwave (MW) transponders could allow for a new and improved means of wirelessly characterizing system properties for the purpose of nondestructive evaluation (NDE). One of the many applications of this potential innovation is

the remote detection of defects in the paneling of aging aircraft. Current structural health monitoring devices employ wire-dependent sensors that must be inconveniently routed and secured without influencing the performance of the system being monitored. We envision that our compact, cost-effective technology could be fully integrated with on-chip piezoelectric sensors and miniaturized antennas. Field implementation would be executed by simply adhering these single-chip devices to monitored structures. These passive components would require no maintenance; their convenient size would easily allow for redundant placement in order to ensure long-term reliability.

As shown in figure 1, microstructural defects could be detected with a bistatic-sonar-like scheme that would be controlled by a centralized, transmitting/receiving (TX/RX) data acquisition unit (DAQ). In response to the command signals of this unit, a voltage controlled oscillator (VCO) would drive an ultrasonic, piezoelectric transducer (XDCR), which would send acoustic waves throughout a monitored structure. The signals received from an array of N integrated circuit (IC) detection nodes would be wirelessly transmitted back to the TX/RX-DAQ station, where a multilateration technique would interpret the data and determine the location and severity of any microfaults in the monitored structure. The acoustic data, $f[t]$, would be encoded in the reflected MW signal by means of phase modulation (PM). By using high-Q resonators as the reactive components of the phase shifting circuits, a specific MW frequency channel (centered on f_r for $r = 1, 2, \cdots, N - 1, N$) could be assigned to each of the N nodes. This frequency-selective identification scheme would allow the TX/RX-DAQ to address individual nodes and extract their data.
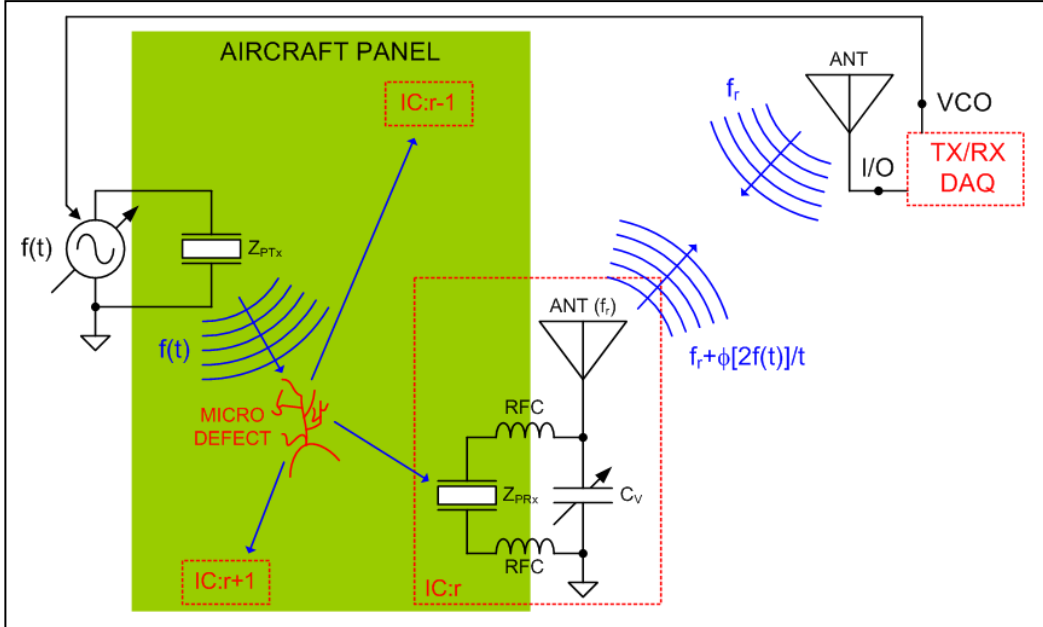
Figure 1. Diagram depicting the role an integrated, backscatter transponder node in a wireless, telemetric, microfault detection system. The nodes modulate the phase component of the reflected MW signal with a received acoustic signal.

An advantage of using PM to transmit analog data across a short range is that this communication scheme is robust against calibration drift due to atmospheric signal attenuation. Traditionally, the military has reserved the L-band, (1 to 2) GHz, for telemetry. There is a strong interest within the wireless community to develop miniaturized, passive S-band transponders (specifically operating in the frequency range of 2.400 to 2.500 GHz) due to the industrial, scientific, and medical (ISM) bandwidth (BW) allocations. However, because our technology is frequency-scalable, the short-range data link needed for our application could reside in C-band (near 5.800 GHz) or K-band (near 24.125 GHz) ISM BW allocations. Operating within the K-band could reduce long-range, electromagnetic (EM) interference with other communication systems—as this particular band is known to experience heavy signal absorption due to atmospheric humidity.

The information detection scheme, shown in figure 1, relies on illuminating passive, backscatter transponders with MW energy. The illumination is transmitted by the TX/RX-DAQ unit, which also performs a pulse compression technique on the backscattered data. The architecture of the TX/RX-DAQ unit is shown in figure 2a. The analog frontend uses an In-Phase (I)/Quadrature (Q) demodulator, shown in figure 2b, which down-converts I and Q signal components. A field-programmable gate array (FPGA) uses digital signal processing (DSP) algorithms to decode echo-location information from the backscattered signal and implement chirped pulse compression via an auto-correlated matched filter function.
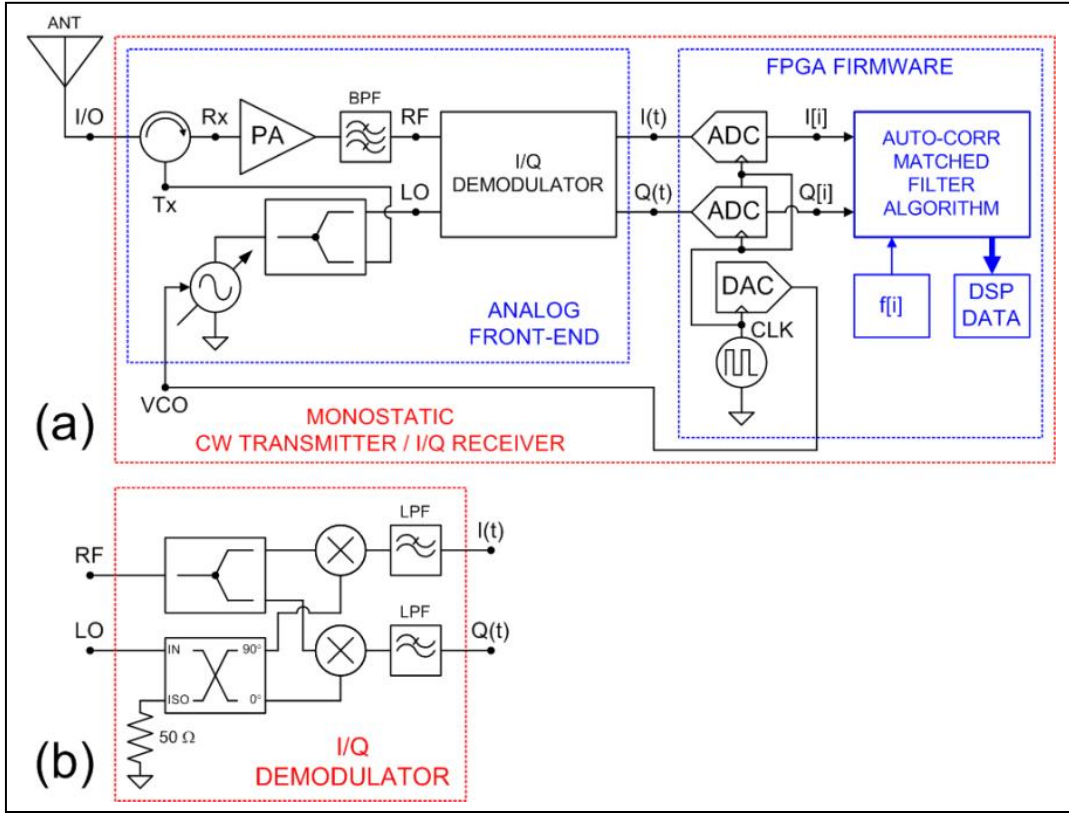
Figure 2. (a) Transceiver architecture and (b) I/Q demodulator circuitry.

3

To realize the individual transponder nodes featured in figure 1, we have envisioned a configuration involving the monolithic integration of a PZT XDCR and a coplanar patch antenna loaded with BST thin film, inter-digital finger capacitor (IDC)-style varactors. The voltage generated by the XDCR modulates the impedance of the IDCs, and consequently, the reflection coefficient of the backscatter transponder. Figure 3a and b depicts the top-side and cross-sectional views of a design involving the use of thin-film PZT. The XDCR is fabricated on the bottom side of a host substrate while the BST IDC loaded antenna is fabricated on its top side. In this approach, the top and bottom electrodes of the XDCR establish a voltage bias across the IDC electrodes by way of highly inductive, through-wafer microvias. Top-side and cross-sectional views of a simpler design (from a micro-fabrication point of view) that uses bulk rather than thin-film PZT is shown in figure 3c and d, respectively. In this design, a wrap-around interconnect is used in place of the microvias. In section 3.3.1, we report on the use of bulk PZT XDCRs in an echo-location demonstration.
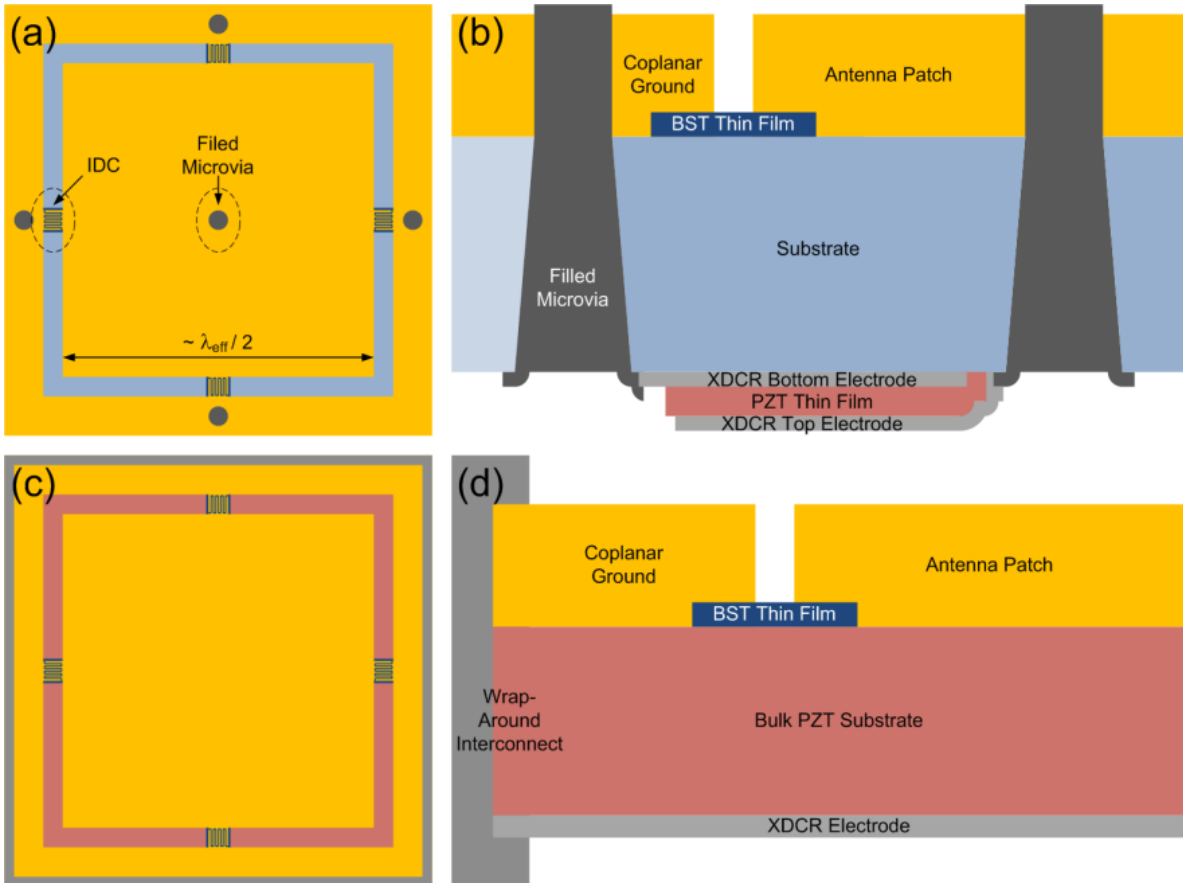
Figure 3. Integrated, backscatter transponder nodes: (a) top-side and (b) cross-sectional views of PZT thin film version, and (c) top-side and (d) cross-sectional view of bulk PZT version.

3. Results

3.1 Third-order Electric-field-induced Dipolar Resonances from Patterned BST Thin Films

There is currently a strong interest within the wireless community to develop low power-loss varactor technologies that can be used for S-band operation—specifically, within the frequency range of (2.400 to 2.500) GHz due to the ISM bandwidth allocations. Such tunable components are sought for use in antenna, transponder, and front-end systems that require agile frequency selectivity or impedance matching optimization. In order to improve the performance of these systems, it is important to fully understand the nature of physical phenomena that give rise to undesired power loss. This section describes the observed electric-field-induced loss mechanisms of thin-film $(Ba_{0.6}Sr_{0.4})TiO_3$ (BST) varactors that reside within the aforementioned frequency band. By investigating how such loss mechanisms behave in response to external stimuli, we have gained insight with respect to how these effects can be reduced or even eliminated. It is also possible that such loss mechanisms could be exploited for the purpose of engineering super-compact, high quality factor, frequency-selective filters.

Previous studies have reported on similar resonant loss mechanisms in paraelectric phase strontium titanate $(SrTiO_3)$ (*2, 3*) and $(Ba_{0.7}Sr_{0.3})TiO_3$ (*3–5*). Such anomalies have been attributed to electric-field-induced piezoelectricity (*2*), electrostrictivity (*4*), and a combination of these two mechanisms (*3, 5*). Some of these studies (*3, 4*) have shown that models based on acoustic impedance calculations yield predictions that qualitatively agree with observed behavior; however, no attempts have been made to accurately model the lineshape of the anomalous resonances in order to extract physical information. We have shown that profiles of such signatures can be precisely fit to simple expressions derived from the Lorentz oscillator model. We have also shown that the extracted dielectric constant has third-order dependence on extrinsic electric field and exhibits excellent agreement with a model derived from a Landau-Devonshire-Ginzberg (LDG) power series expansion.

As depicted in figure 4a, metal-insulator-metal (MIM) varactors were fabricated from BST thin films with measured thicknesses of $h = (240 \pm 10)$ nm and having compositions of $Ba_{0.6}Sr_{0.4}TiO_3$. The films were grown via the metal organic solution deposition (MOSD) technique using carboxylate-alkoxide precursors. A detailed description of the MOSD precursor solution preparation and film deposition technique has been previously reported (*6*). The BST films were deposited on platinum (Pt) blanket layers (with nominal thicknesses of 200 nm) adhered to 300-µm-thick c-plane sapphire (Al_2O_3) substrates with thin titanium adhesion layers (of approximately 40 nm in thickness). In the presence of flowing oxygen, the BST films were crystallized using conventional furnace annealing (CFA) at a temperature of 750 °C for a duration of 60 min. Following the CFA process, these films were ultraviolet (UV)-irradiated for

225 min in an oxygen atmosphere held at a temperature of 700 °C, as described in previously published literature (*7*). The BST thin films were then lithographically masked with Microposit SC-1827 photoresist and etched with buffered oxide etchant (5:1:ammonium fluoride [NH$_4$F]:hydrofluoric acid [HF]). Finally, 200-nm-thick gold electrodes were sputtered over the etch-defined patches of BST and patterned using conventional optical lithography and lift-off methods. This processing step defined both the top electrode and bottom electrode probe landing pads. The primary dimensions of concern of the varactors include diameter d, dielectric/metal overlap L$_{OV}$, and signal-to-ground spacing L$_{SP}$. For the characterizations presented in this study, values of L$_{OV}$ = (15.0 ± 2.0) µm and L$_{SP}$ = (50.0 ± 0.05) µm were held fixed for each measurement; the accuracies of these two values are due to mask alignment error and optical lithography mask resolution, respectively. The parameter d was used as a variable in our experiments and took on values of (22.4, 70.9, and 128.95) µm ± 0.1 µm. These values were chosen so as to minimize network analyzer error by satisfying the relationship: $\left| Z \right| \approx (2\,\pi\,f\,C)^{-1} \sim 50\,\Omega$ where $\left| Z \right|$ is the measured device under test (DUT) impedance magnitude, f is test signal frequency, and C is the extracted DUT capacitance.

Figure 4b illustrates the measurement scheme that was used for extracting material parameters from the test structures at MW frequencies. The DUT impedance values were measured using MW reflection spectrometry obtained from an Agilent Technologies E8364C PNA Series network analyzer, as illustrated in figure 4b. The DUT was contacted using a GGB Industries model 50A-GS-150-P high performance MW probe. The fictitious reference plane (defined at $z = 0$), which separates the apparatus from the DUT, was established using a set of short-open-load (SOL) standards from a GGB Industries CS-8 calibration substrate. A DC voltage (V_{DC}) was established across the top and bottom electrodes, using an Agilent Technologies PNA Option UNL bias-tee and a Yokogawa 7651 programmable DC source, for the purpose of biasing the BST thin film with an extrinsic electric field ($E_{DC} \approx -V_{DC}/h$). In all reported experiments, the MW small-signal power level was held fixed at a value of −30 dBm. When extracting the real part of the relative permittivity, we have used the approximation $\epsilon'_{r,TOT} \approx (4\,C\,h)/(\pi\,\epsilon_0\,d^2)$. This assumption, which neglects the influence of fringe field on the measured value of C, is appropriate (*8*) because, for each characterized DUT, $d \gg 2\,h$. Likewise, we have extracted the imaginary part of the relative permittivity using the approximation $\epsilon''_{r,TOT} \approx \epsilon'_{r,TOT} \tan \delta_\epsilon$, where $\tan \delta_\epsilon$ is the measured dielectric loss tangent. The accuracy of the reported relative permittivity values Δ_ϵ can be readily calculated assuming the capacitance, diameter, and film thickness measurements are entirely independent of one another—allowing for all covariant terms to vanish (*9*). In our measurements, the error term associated with the capacitance measurement is considerably smaller than those of the diameter and film thickness measurements, yielding the approximation $\Delta_\epsilon^2 = {\epsilon'_{r,TOT}}^2 \left(\frac{\Delta_C^2}{C^2} + \frac{\Delta_h^2}{h^2} + \frac{4 \cdot \Delta_d^2}{d^2} \right) \approx {\epsilon'_{r,TOT}}^2 \left(\frac{\Delta_h^2}{h^2} + \frac{4 \cdot \Delta_d^2}{d^2} \right)$.
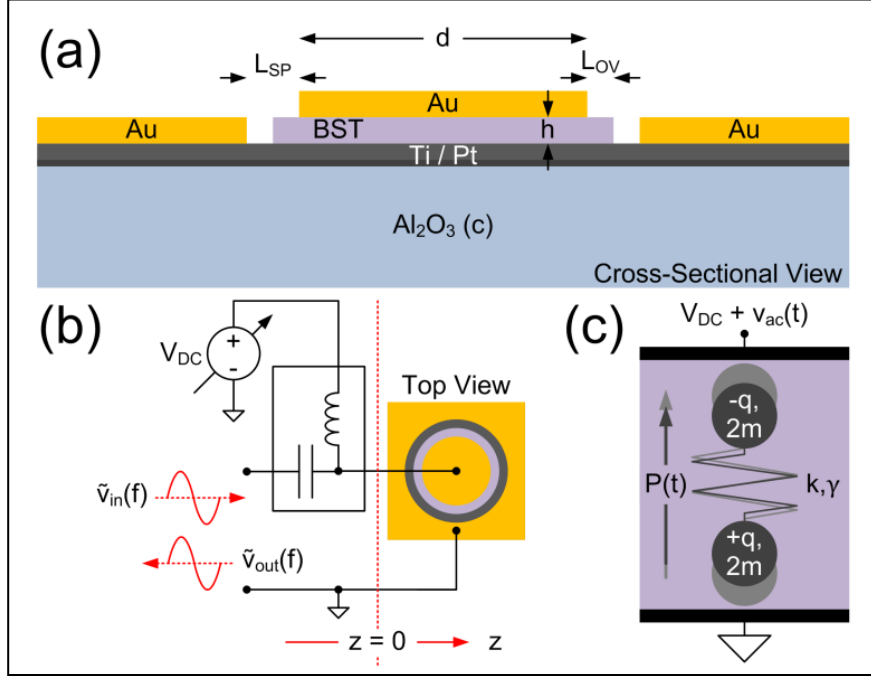
Figure 4. (a) Cross-sectional depiction of BST-based MIM capacitor for MW characterizations. (b) Single-port MW reflection apparatus for characterizing electronic material properties (complex permittivity) at MW frequencies. (c) Effective model of an ensemble of resonating dipolar domains.

To mathematically model electric-field-induced electro-acoustic resonances, we first consider that the net polarization of a BST thin film is the vector summation of individual electric dipole moments contributed from N polarizable domains (which individually exhibit paraelectric behavior), $\bar{P} = \sum_{i=1}^{N} \bar{\mu}_i$. To first order, we reduce this calculation to $P = N\mu$ where μ is the mean electric dipole moment, and statistical variance has been neglected. We propose that the equation of motion that governs the behavior of P is that of a classical harmonic oscillator driven by an alternating, small-signal, electric field E_{ac} (the Lorentz oscillator model):

$$\ddot{P} + 2\pi\Gamma\dot{P} + \omega_0^2 P = \frac{N q^2}{m} E_{ac} e^{i\omega t}. \tag{1}$$

In this expression, we have used the substitution of $2\pi\Gamma \equiv \gamma/m$ where m is the reduced, effective mass and γ is the damping constant of the harmonic oscillator. The angular resonant frequency ω_0 has also been substituted into this expression using the relation $\omega_0^2 \equiv k/m$ where k is the effective Hooke spring constant. The quantity q is the displaced charge associated with P. A literal interpretation of the effective model represented by equation 1 is shown in figure 4c. In this picture, the biasing electric field (produced by V_{DC}) induces an electric dipole moment that oscillates in response to a small time-dependent signal $v_{ac}(t)$. Historically, this concise mathematical model has been used to describe dipolar resonant phenomena arising from optical phonon excitation (10) in barium titanate (BaTiO$_3$) and SrTiO$_3$ in addition to numerous examples of complex permittivity (11).

7

By solving equation 1 and applying the relations for complex electric susceptibility and permittivity—$\chi = \epsilon_0^{-1}(dP/dE) = P/(\epsilon_0 E_{ac})$ and $\epsilon_r = 1 + \chi$, respectively—we derive expressions for the real part of ϵ_r:

$$\epsilon_r' = 1 + \frac{1-v^2}{(1-v^2)^2+(v/Q_0)^2} \cdot \left(\epsilon_{r,0} - 1\right) \tag{2}$$

and its imaginary counterpart:

$$\epsilon_r'' = \frac{v/Q_0}{(1-v^2)^2+(v/Q_0)^2} \cdot \left(\epsilon_{r,0} - 1\right). \tag{3}$$

These expressions are given in terms of the normalized frequency $v \equiv f/f_0$. For practical purposes, we use cyclic frequency ($f = 2\pi/\omega$, expressed in units of GHz) rather than angular frequency. The other substituted variables include the dimensionless quantities of the DC static dielectric constant ($\epsilon_{r,0} = \epsilon_r[v = 0]$) and the ratio $Q_0 \equiv f_0/\Gamma$ which asymptotically approaches a quantity commonly known as the quality factor— $Q_0 \approx f_0/\Delta f$ for $f_0 \gg \Gamma$ where Δf is the *full width at half maximum* of the ϵ_r'' resonant lineshape. As expected from the Lorentz model, $\epsilon_{r,0} = 1 + \omega_p^2/\omega_0^2$ where $\omega_p{}^2 \equiv (N q^2)/(\epsilon_0 m)$ which is the square of the quantity historically known as the *plasma frequency* for the case of a free ionized gas (i.e., $k \to 0$ and $\gamma \to 0$).

Figure 5a and b shows the real and imaginary parts of the complex permittivity measured over the frequency range of (1 to 4) GHz for extrinsic electric field values of $E_{DC} = (41.67 \pm 1.74, 62.50 \pm 2.60, 104.2 \pm 4.3, 166.7 \pm 6.9, 260.4 \pm 10.9,$ and $416.7 \pm 17.4)$ kV/cm. These measurements were taken at a nominal substrate temperature of $T = (297.65 \pm 0.62)$ K from a device with a top-electrode diameter of $d = (22.4 \pm 0.1)$ μm. As the extrinsic electric field is increased in magnitude, a dielectric relaxation profile and a Lorentzian-like resonant lineshape, respectively, emerge from the real and imaginary parts of the complex permittivity. For electric field magnitudes greater than (104.2 ± 4.3) kV/cm, the data sets could be fit to the functions $\epsilon_{r,TOT}' = \epsilon_{r,BG}' + \epsilon_r'$ and $\epsilon_{r,TOT}'' = \epsilon_{r,BG}'' + \epsilon_r''$ where ϵ_r' and ϵ_r'' are given by equations 2 and 3, and $\epsilon_{r,BG}'$ and $\epsilon_{r,BG}''$ are permittivity backgrounds that can be expressed in terms of power series expansions— $\epsilon_{r,BG}' = a_0 + a_1 f + a_2 f^2$ and $\epsilon_{r,BG}'' = b_0 + b_1 f + b_2 f^2$. The decreasing frequency-dependent trends of these functions are due to a low-pass filtering effect known as high-frequency roll-off and are typical behaviors of BST thin films (*12*). However, the signatures of dipolar resonance generally result from domain-scale mechanisms (*11*) (including those of deformation and orientation polarization). Since dielectric functions resulting from parallel mechanisms are additive, we can justify subtracting the background curves in order to isolate and study these resonant signatures.
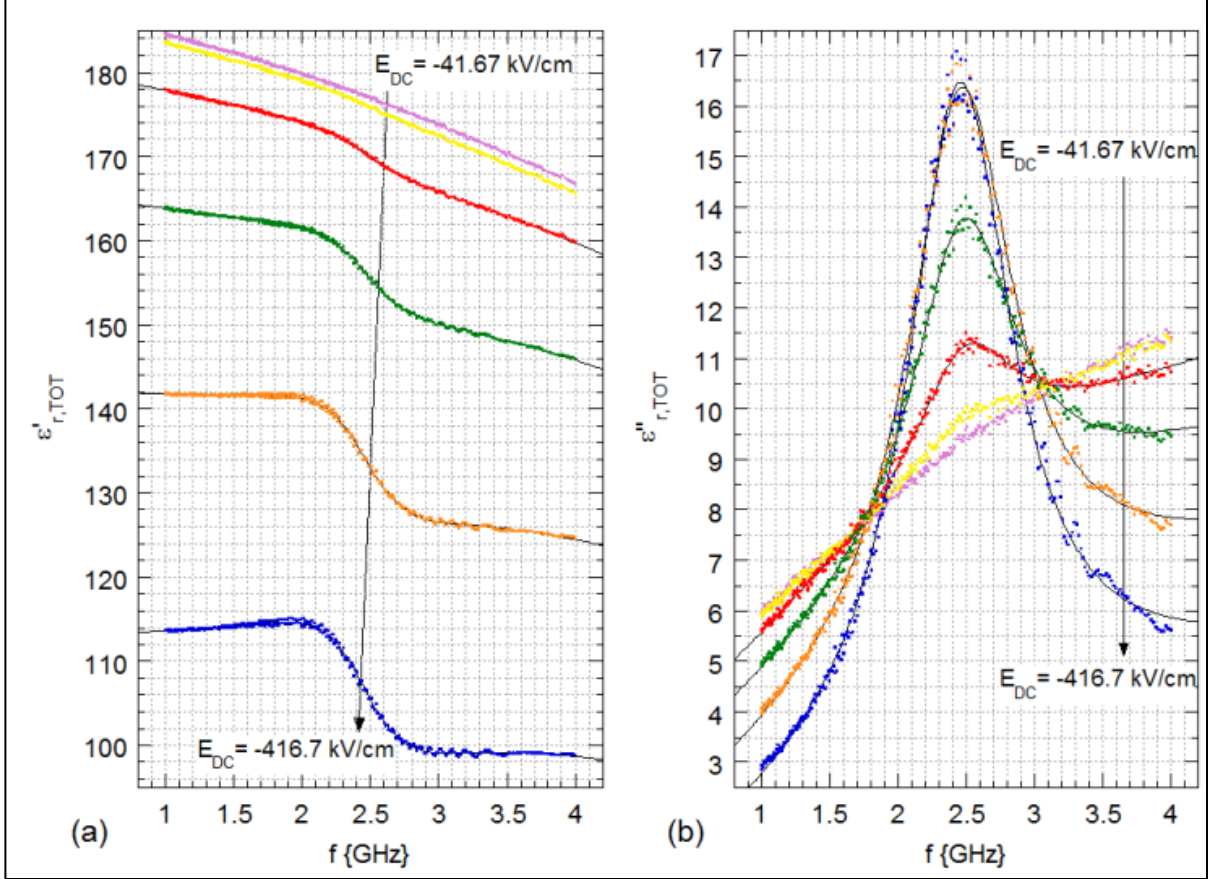
Figure 5. (a) Real ($\epsilon'_{r,TOT}$) and (b) imaginary ($\epsilon''_{r,TOT}$) parts of total permittivity vs. frequency f for a device with a top-electrode diameter of $d = 22.4$ μm measured at a nominal temperature of $T = (297.65 \pm 0.62)$ K for different values of extrinsically applied electric field E_{DC}.

The size and temperature dependence of the resonant signatures are shown in figure 6a and b, respectively. In figure 6a, the real and imaginary parts of the total permittivity have been recorded at the nominal temperature and curve-fit as functions of frequency for devices having top electrode diameters of $d = (22.4,\ 70.9,\ \text{and}\ 129.5)$ μm $\pm$ 0.1 μm. These three devices were fabricated on the same microchip in close proximity to one another so as to eliminate the influence of run-to-run process variation and reduce the influence of film thickness variation. In figure 6b, the real and imaginary parts of the total permittivity have been recorded from the smallest device and curve-fit as functions of frequency for substrate temperatures of $T = (297.65 \pm 0.62, 370.75 \pm 0.70, \text{and}\ 467.35 \pm 0.79)$ K. For both sets of measurements, the extrinsic electric field bias was held fixed at $E_{DC} = (-416.7 \pm 17.8)$ kV/cm. From the data, it is evident that the resonant signature becomes more distinct as the device size is reduced; the fitting parameter Q_0 (the lineshape figure of merit) increases with values of 0.9837 ± 0.0434, 2.318 ± 0.049, and 2.669 ± 0.038. On the contrary, temperature has little to no influence on the value of Q_0 which was observed to proportionally (albeit slightly) increase with values of 2.669 $\pm$ 0.038, 2.675 $\pm$ 0.041, and 2.683 $\pm$ 0.036. Since these values are within each other's range of error, there is no reportable trend. Similarly, neither device size nor temperature drastically

9

influenced the value of f_0. For increasing device size, the values of f_0 were measured as (2.495 ±0.002, 2.391 ± 0.004, and 2.409 ± 0.039) GHz. For increasing temperature, the values of f_0 were found to be: (2.495 ± 0.002, 2.522 ± 0.002, and 2.510 ± 0.002) GHz. Previous studies have shown that the value of f_0 is primarily governed by thin-film thickness (4).
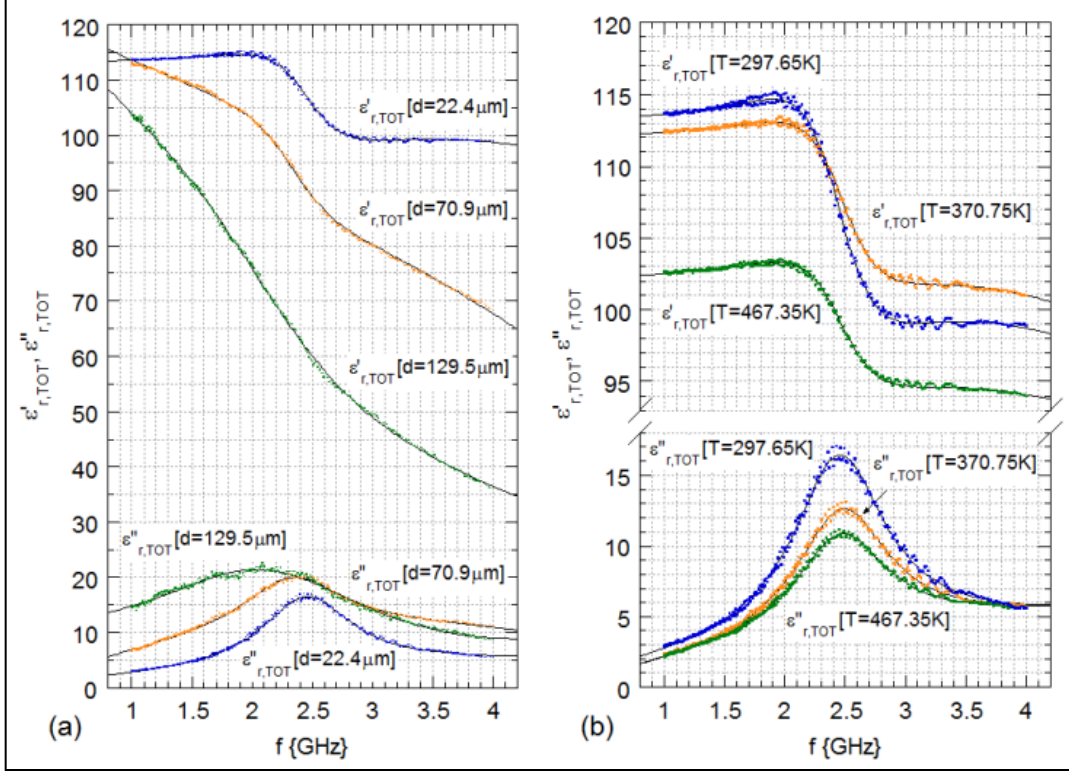
Figure 6. (a) Real ($\epsilon'_{r,TOT}$) and imaginary ($\epsilon''_{r,TOT}$) parts of total permittivity vs. frequency f for devices of different sizes $d = 22.4$ μm, 70.9 μm, and 129.5 μm) measured at a nominal temperature of $T = (297.65 \pm 0.62)$ K with an extrinsic electric field biases of $E_{DC} = -416.7$ kV/cm. (b) Real ($\epsilon'_{r,TOT}$) and imaginary ($\epsilon''_{r,TOT}$) parts of total permittivity versus frequency f for a device with a top electrode diameter of $d = 22.4$ μm biased at $E_{DC} = -416.7$ kV/cm and measured at different temperatures.

In figure 7, the extracted fitting parameters $\epsilon_{r,0}$ have been plotted as a function of extrinsic electric field magnitude E for the size and temperature conditions of figure 6a and b. Data from the two larger devices exhibit inverse proportionality with E while we found that data from the smallest device could be fit to an expression derived from the LGD model. For non-polar centrosymmetric phases, a third-order power series expansion of odd terms (13) can be assumed for the electric-field-polarization relationship, $E = \alpha_1 P + \alpha_3 P^3 + \cdots$. It should be noted that the coefficients α_1 and α_3 can be solely attributed to linear and nonlinear dielectric stiffness, respectively. However, it has been theorized that two-dimensional mechanical clamping of the thin film to the substrate results in renormalization of these constants with added terms involving electrostriction and elastic compliance tensor elements (14, 15).
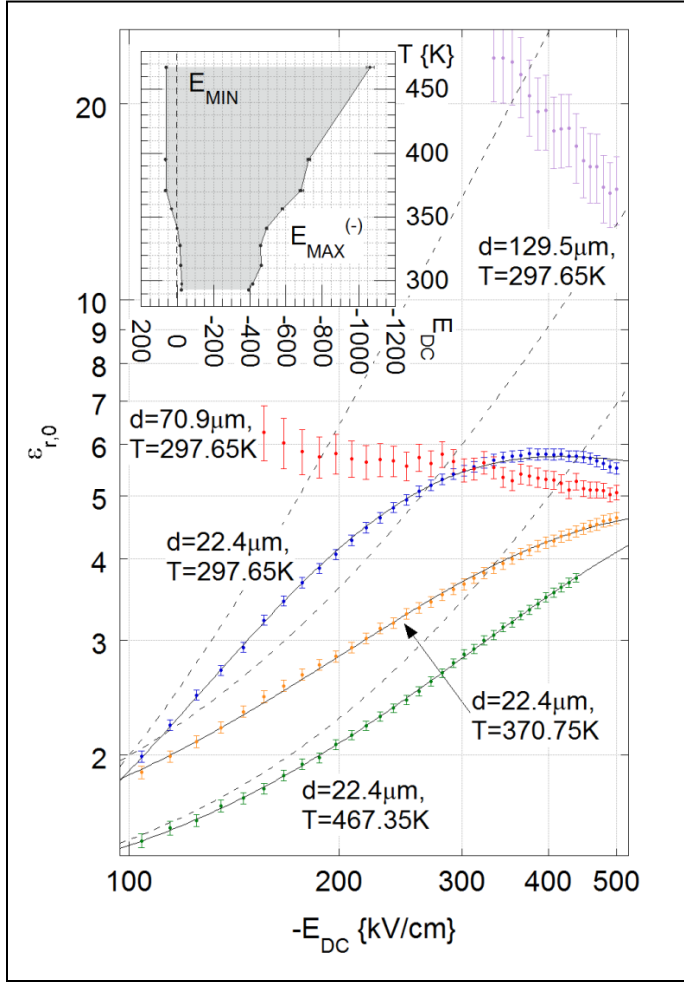
Figure 7. Extracted static dielectric constant $\epsilon_{r,0}$ vs. extrinsicelectric field bias E_{DC} for a device of size $d = (22.4 \pm 0.1)$ μm at substrate temperatures of $T = (297.65 \pm 0.62, 370.75 \pm 0.70, 395.15 \pm 0.72, 467.35 \pm 0.79)$ K. and devices of sizes $d = (70.9 \pm 0.1$ and $129.5 \pm 0.1)$ μm at a nominal temperature of $T = (297.65 \pm 0.62)$ K. Data sets are colored blue, orange, green, red and violet, respectively. Inset shows the regime bounded by $E_{MAX}^{(-)} \leq E_{DC} \leq E_{MIN}$ for curves fitted to data sets collected at $T = (293.05 \pm 0.62, 297.65 \pm 0.62, 312.25 \pm 0.64, 327.45 \pm 0.65, 341.05 \pm 0.67, 356.45 \pm 0.68, 370.75 \pm 0.70, 395.15 \pm 0.72, 467.35 \pm 0.79)$ K. In both graphs, the error bars represent the standard error values resulting from nonlinear curve fitting methods.

By using the method of Chase (*16*), the LGD expansion can be inverted in terms of E:

$$P[E] = \frac{3}{2}\epsilon_0 \chi_{MAX} E_2 \sinh\left[\frac{1}{3}\sinh^{-1}\left[\frac{2E}{E_2}\right]\right] \tag{4}$$

where χ_{MAX} is the zero-bias susceptibility and E_2 is an electric field scaling factor (*16*). From this expression, the nonlinear susceptibility for small signals ($E_{ac} = E - E_{DC}$) can be expressed in terms of a Taylor series expansion centered about the quiescent point $E = E_{DC}$:

$$P[E_{DC}, E_{ac}] = \epsilon_0 \left\{ \chi_1[E_{DC}]\, E_{ac}[t] + \chi_2[E_{DC}]\, E_{ac}^2[t] + \chi_3[E_{DC}]\, E_{ac}^3[t] + \cdots \right\}. \tag{5}$$

11

The first- and third-order susceptibility terms, calculated with the equation $\chi_n[E_{DC}] = \frac{1}{\epsilon_0 n!} \frac{d^n P[E]}{dE^n}\Big|_{E=E_{DC}}$, are respectively

$$\chi_1[E_{DC}] = \chi_{MAX} \left(2 \cosh\left[\frac{2}{3} \sinh^{-1}\left[\frac{2E_{DC}}{E_2} \right] \right] - 1 \right)^{-1} \tag{6}$$

and

$$\chi_3[E_{DC}] = \chi_{3,0} + \frac{32}{9} \frac{\chi_{MAX}}{E_2^2} \left(5 \left(\frac{\chi_1[E_{DC}]}{\chi_{MAX}} \right)^4 - 6 \left(\frac{\chi_1[E_{DC}]}{\chi_{MAX}} \right)^5 \right). \tag{7}$$

Our observations from figure 5 suggest that the biased-induced resonance should be subject to the boundary condition $\chi_3[0] = 0$. For this reason, we have rationalized adding a constant term $\chi_{3,0} = 32\chi_{MAX}/(9E_2^2)$ to equation 7. Experimentally, we have collected reflectometry from the DUT using a single-frequency small-signal whose electric field can be represented by $E_{ac}[t] = E_{ac,0} \cos[2\pi ft]$ where $E_{ac,0}$ is the signal's magnitude. The partial polarization resulting from the third-order susceptibility, is therefore

$$P^{(3)}[E_{DC}, E_{ac}] = \epsilon_0 \, \chi_3[E_{DC}] \left(\frac{3}{4}\cos[2\pi ft] + \frac{1}{4}\cos[2\pi(3f)t] \right) E_{ac,0}^3. \tag{8}$$

Since our apparatus only measures the first-order frequency f reflection, and not that of the third-order harmonic $3f$, the effective third-order susceptibility should be written as $\chi_{3,eff}[E_{DC}] = \frac{3}{4} E_{ac,0}^2 \chi_3[E_{DC}]$. It follows that the extracted function of $\epsilon_{r,0}$ from the frequency-dependent measurements of ϵ_r' and ϵ_r'' should have the form of

$$\epsilon_{r,0}[E_{DC}] = 1 + \frac{8}{3}\left(\frac{E_0}{E_2}\right)^2 \left(1 + 5\left(\frac{\chi_1[E_{DC}-E_{MIN}]}{\chi_{MAX}} \right)^4 - 6\left(\frac{\chi_1[E_{DC}-E_{MIN}]}{\chi_{MAX}} \right)^5 \right) \tag{9}$$

where $E_0 \equiv \chi_{MAX}E_{ac,0}^2$. This function has extrema occurring at $E_{DC} = E_{MIN}$ and $E_{DC} = E_{MAX}^{(\pm)} \equiv E_{MIN} \pm \frac{7\sqrt{2}}{16}E_2$. The maxima $E_{MAX}^{(\pm)}$ represent polarization saturation points. E_{MIN} is an experimentally observed electric field offset. Similar shifts from first-order capacitance-voltage (C–V) measurements have been attributed to strain gradients (12) possibly resulting from asymmetries of the electrode and probe configurations. It is also likely that signal rectification resulting from even-order terms in the expansion of equation 5 contribute this offset. In the regime of weak polarization, $|E_{DC} - E_{MIN}| \ll |E_2|$, equation 9 can be approximated by a simple quadratic expression:

$$\epsilon_{r,0}[E_{DC}] \approx 1 + \frac{1280}{27}\left(\frac{E_0}{E_2}\right)^2 \left(\frac{E_{DC}-E_{MIN}}{E_2}\right)^2. \tag{10}$$

As shown in figure 7, equation 9 accurately models the E_{DC}-dependent behavior of the data collected from the $d = 22.4$ μm device. The inset shows a *gray region*, bounded by $E_{MAX}^{(-)} \leq E_{DC} \leq E_{MIN}$ for the substrate temperatures ranging from $T = (293.05 \pm 0.62)$ K to (467.35 ± 0.79) K. An anomalous feature of this plot is the fact that the E_{MIN} and $E_{MAX}^{(-)}$ do not appear to be a linear functions of temperature; near $T = (341.05 \pm 0.67)$ K there is an unexplained sign

reversal of E_{MIN}. However, the general trend shows that the regime of weak polarization broadens with increasing temperature. This observation suggests that thermal phonon interaction causes individual resonating domains to desynchronize from the net resonance of the collective ensemble. To illustrate this point, the dashed lines of figure 7 are the approximations of equation 10 for fitted curves corresponding to temperatures of $T = (297.65 \pm 0.62, 370.75 \pm 0.70, 395.15 \pm 0.72, 467.35 \pm 0.79)$ K. At the highest temperature, the data approaches the quadratic approximation for relatively low values of E_{DC}.

We have observed an anomalous resonance with third-order dependence on extrinsically applied E_{ac}. We have characterized this signature using a model that assumes the net resonance arises from an ensemble of resonating polarized domains. Our studies demonstrated that the extracted parameter Q_0 is inversely proportional to the device size—larger devices (which contained a greater number of individual dipole moments) exhibited broader resonant profiles. This observation suggests that statistical variation in grain size and orientation significantly influence the collective coherence of the composite resonator. Additionally, it is possible that two-dimensional mechanical clamping of the device to the nearly rigid sapphire substrate could also reduce the value of Q_0. Although this figure of merit and f_0 were relatively temperature-insensitive, the regime of weak polarization associated with $\epsilon_{r,0}[E_{DC}]$ broadened significantly as the substrate temperature was increased. This trend is likely due to desynchronization of individual resonating dipoles caused by thermal phonon interaction.

Previous investigators have observed similar resonant anomalies, which they attributed to E_{DC}-induced piezoelectricity (*2*), electrostrictivity (*4*), and a combination of these two mechanisms (*3, 5*). Our mathematical model, derived from a simple third-order LGD power series expansion, implies that the resonant phenomena simply arise from the nonlinear $P - E$ relationship, which can result from nonlinear dielectric stiffness alone—although it is likely that other mechanisms including piezoelectricity and electrostrictivity contribute to this effect. Consequently, partial polarization signatures of all integer orders of magnitude should be observable. For clarity, piezoelectric and electrostrictive displacement (and therefore polarization) are mathematically described (*17*) as having first- and second-order dependence on E_{ac}, respectively. We were able to indirectly detect third-order resonant behavior using a linear measurement (a swept single-frequency technique) only because of the fact that the third-order susceptibility produces a first-order signature. We eliminated the influence of first-order susceptibility from this measurement when we subtracted the background dielectric functions from the real and imaginary parts of the measured complex permittivity. Direct measurements of harmonic distortion would be required to truly characterize second-order susceptibility (commonly associated with electrostriction).

3.2   Lead Zirconate Titanate Thin-film Characterizations

A novel thin-film $Pb_{1+y}[Zr_xTi_{1-x}]O_{3+y}$ (PZT) ultrasonic detector (UD) was realized using a MIM configuration. This device was fabricated by sputtering 820 Å of Pt followed by 6146.8 Å of PZT over a 3-in-diameter, <100> silicon (Si) wafer. Subsequent to this in situ processing step,

an additional 1050 Å Pt thin film was sputtered over a shadow mask placed in direct contact with the Pt/PZT blanket layer to form an array of 1 mm × 1 mm top electrodes. The wafer was then annealed using rapid thermal annealer (RTA) at a temperature of 700 °C. A masked portion of the exposed PZT thin film was etched away, using a buffered oxide etchant (BOE), to expose the bottom electrode for electrical contact.

To prepare the MIM structures for ultrasonic detection in aircraft-grade Al beams, the samples were cleaved by hand using a diamond scribe and straight edge. Using silver conductive paste (Alfa Aesar 42469), 134-AWP solid copper wires (Vishay Precision Group F006484) were connected to the bottom electrodes of the samples, which were intended for *face-down* adhesion to the Al beams, as shown in figure 8a. Figure 8b displays this devices's frequency-dependent capacitance and dielectric loss tangent from 100 Hz to 40 MHz with zero voltage bias. The increase in loss tangent in the neighborhood of (3 to 5) MHz suggests resonant behavior. As shown in figure 8c and d, voltage-dependent capacitance and dielectric loss tangent measurements were performed the thin-film PZT UDs using a Hewlett-Packard 4194A impedance gain-phase analyzer. These measurements were obtained using a 10-kHz test signal with an amplitude of 0.05 V root mean square (RMS). Both characterizations featured sweep-direction-dependent hysteresis—possibly due to a combination of both piezoelectric and ferroelectric polarization.
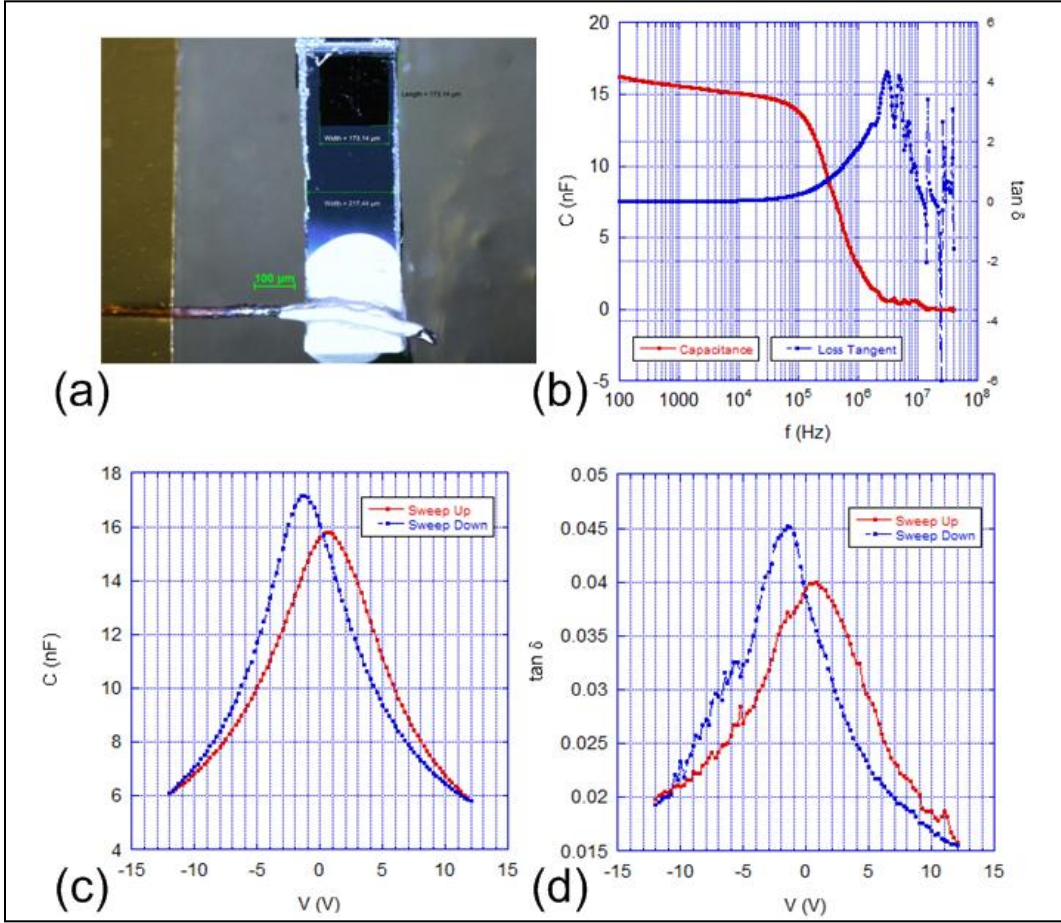
Figure 8. (a) Thin-film PZT UD prepared for face-down adhesion. (b) Capacitance and dielectric loss tangent vs. frequency. (c) Capacitance and (d) dielectric loss tangent vs bias voltage.

A similar device was adhered to an Al beam in a *face-down* configuration—as shown in figure 9a. Figure 9b shows the zero-bias, frequency-dependent capacitance and dielectric loss tangent from 100 Hz to 40 MHz. Figure 9c and d shows the voltage-dependent capacitance and dielectric loss tangent, respectively, at 10 kHz.
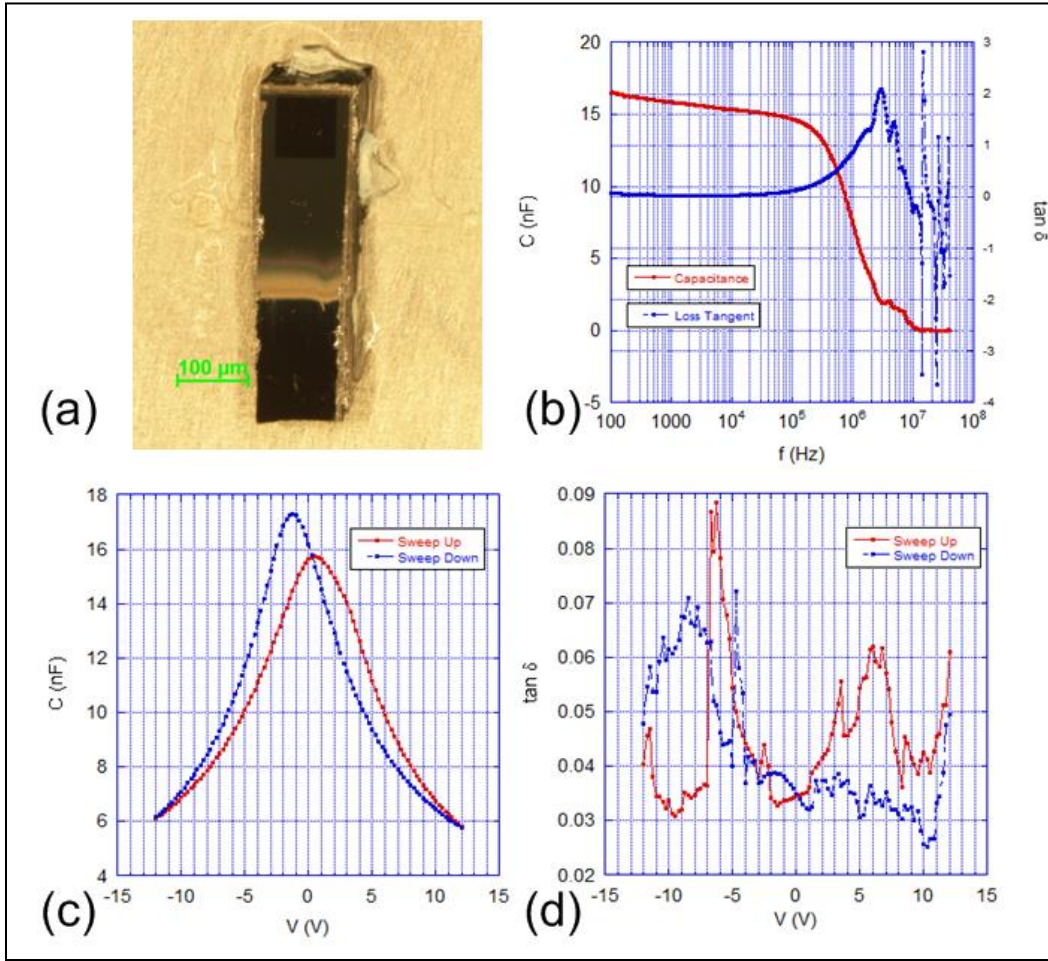
Figure 9. (a) Thin film PZT UD prepared for face-up adhesion. (b) Capacitance and dielectric loss tangent vs. frequency. (c) Capacitance and (d) dielectric loss tangent vs. bias voltage.

3.3 Nondestructive Evaluation Demonstrations

3.3.1 Acoustic Nondestructive Evaluation of Aircraft Paneling

A NDE system for monitoring structural health in aircraft paneling was constructed and tested. The system relies on the use of commercially available piezoelectric wafer active sensors (PWASs)—as described in previously published literature (*18*). These sensors were bonded to 0.063-in-thick, aircraft-grade, high-strength Al (Alloy 2024) sheets using commercially available strain gauge adhesive, and 22 AWG hook-up wire was soldered to each one in order to establish electrical contact. Audio and ultrasonic, burst-modulated sinusoidal signals were applied to a single PWAS using an arbitrary waveform generator. The acoustic response was detected by the remaining sensors and measured using an oscilloscope. Location of defects in the aircraft paneling was determined using a multilateration algorithm based on a cross-correlation technique. In order to test the detection limits of our NDE system, holes with a variety of diameters were intentionally drilled through the aluminum panels. The system was able to detect holes with diameter sizes that were comparable to the panel thickness. Figure 10a features the

oscilloscope screenshot from an experimental apparatus shown in figure 10b. Four waveforms are shown. The top waveform represents the input signal provided by the AWG and fed to a PWAS XDCR. The remaining three waveforms represent the electrical signals received at the three PWAS sensor nodes. A cross-correlation algorithm was implemented to triangulate the position of holes that were drilled into aircraft-grade Al panel. Additional details regarding these experiments are described in a 2011 Science & Engineering Apprentice Program (SEAP) report (*19*).
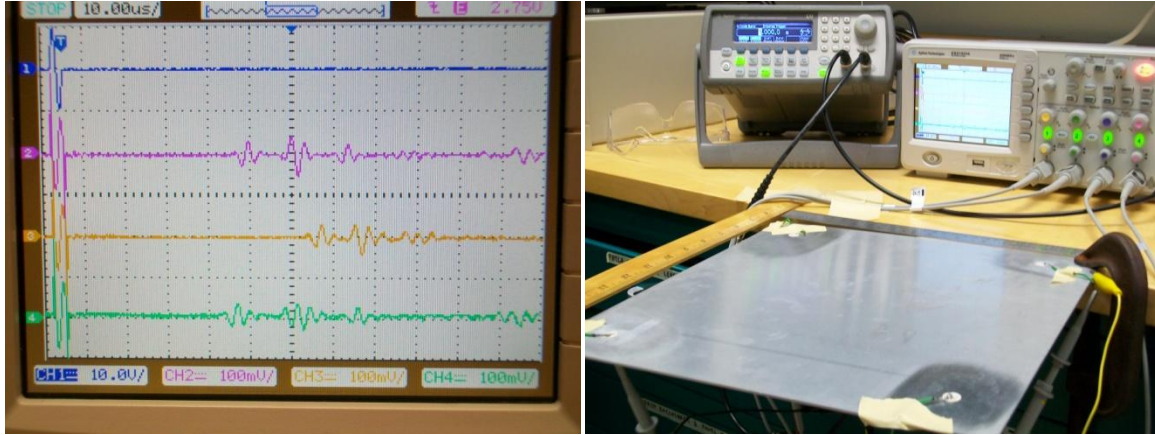


Figure 10. (a) Oscilloscope screen-shot featuring electrical read-out of transmitted and received acoustic signals. (b) NDE appartus demonstrating the utility of PWAS XDCRs.

3.3.2 Ultrasonic Detector Demonstrations

To demonstrate the use of the thin-film PZT as a viable material for structrual health monitoring applications, the thin-film PZT UDs were used to sense acoustic signals generated by commercially available PWAS. The use of such bulk piezoelectric material for both acoustic transmission and reception has been thoroughly investigated by previous researchers (*18*). The thin film PZT UDs were bonded in *face-down* and *face-up* orientation to the aircraft-grade Al (alloy 2024-T4) beams using strain gauge adhesive (Vishay Precision Group M-Bond 200).

Figure 11a is a photograph of the experimental configuration for testing the thin-film PZT UDs in the *face-down* orientation. A 9.5 in × 1 in × 1/8 in beam was C-clamped to a laboratory bench to create a 7 1/8-in-long cantilever. The thin-film PZT UD was adhered to the Al so that its top electrode was placed in direct contact with the beam while the exposed portion of its bottom electrode was suspended off the beam's end. Two PWASs were also fixed to the beam. The first was placed at an approximate distance of 1 3/16 in away from the thin-film PZT UD, the second was placed at an equal distance on the opposite side of the first. A common electrical grounding point for all three devices was established by positiong an alligator clip at the beam's clamped end. An Agilent 33220A arbitrary waveform generator was used to apply a voltage signal V_{in}, driven ultrasonic frequencies, to the top electrode of the first PWAS. A voltage response V_{out} was generated at the bottom electrode of the thin-film PZT UD and the top

17

electrode of the second PWAS; these signals were acquired and recorded using an Agilent DSO1024A 200-MHz oscilloscope. The resulting transfer functions of each piezoelectric receiver are shown in figure 11b for comparison. We have defined the frequency-dependent transfer function as the scaled logarithm of the ratio of received-to-sourced signals ($T[f] = 20$ $Log_{10}[V_{out}/V_{in}]$ {dB}). The two curves are similar in response with that of thin-film PZT UD being between weaker, within a few decibels, than that of the PWAS. Each response features an on-resonant peak near 7.5 MHz. Although the greater-than-unity gain of the on-resonant response of the PWAS is seemingly counterintuitive, this effect most likely resulted from simple transformer action related to placement along the cantilevered beam.
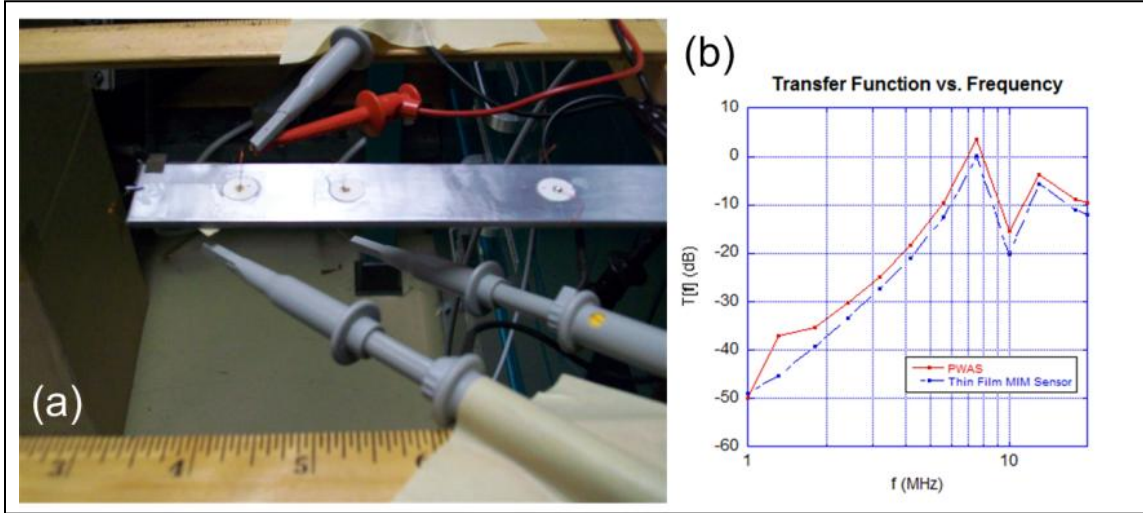
Figure 11. Face-down experiment: (a) test configuration and (b) transfer functions of PWAS and the thin-film PZT UD.

An experiment with the thin-film PZT UD positioned in a *face-up* orientation is shown in figure 12a. This test configuration was more convenient to perform from a technical aspect as no wire pasting was required. The thin-film PZT UD was placed approximately 2.303 in (58.5 mm) away from a PWAS along a 5 in × 1 in × 1/16 in Al beam of an unknown alloy. The beam was not clamped at any point, but simply placed on top of an aluminum base. In this experiment, micro-positioner probes were used to transmit acoustic signal from the PWAS; the acoustic response was detected by the thin-film PZT UD. The resulting transfer function is shown in figure 12b with a resonant peak at 5.6 MHz. This attenuation of this response is greater than 5 dB. It is currently unclear as to whether this increased power dissipation is due dampening in the Al base or the Si wafer. Regardless, the detection of an acoustic signal with an integrated Si-based sensor is a promising result.
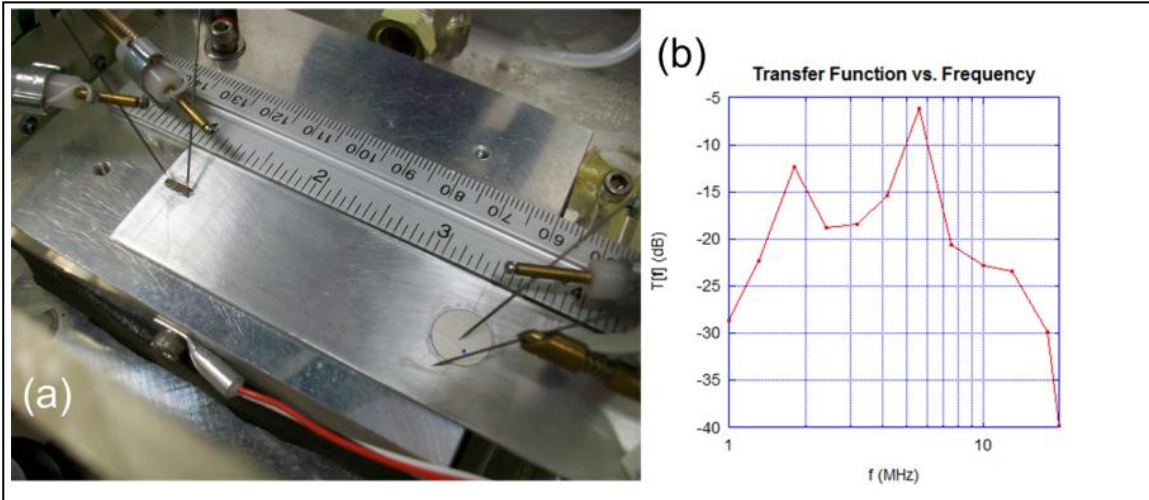
Figure 12. Face-up experiment: (a) test configuration and (b) transfer function of the thin-film PZT UD.

4.   Conclusion

In this body of work, we have explored the electrical properties of BST and PZT thin films. In doing so, we have discovered interesting phenomena involving third-order electric-field-induced dipolar resonances in our fabricated using the MOSD process. Since this anomalous behavior was not well understood, we took a *short detour* from the main objective of the project in order to investigate and understand more about the physics of electro-acoustic coupling in our thin films. We did not find enough time to monolithically integrate BST and PZT within the two-year time frame of the DRI project—which was one of the initially proposed objectives. However, we did successfully implement a NDE detection scheme involving bulk PWAS XDCRs and we performed some preliminary experiments that demonstrated the use of thin-film PZT as an acoustic sensor.

Overall, this project was a success. The seed funding provided by the DRI has created the internal infrastructure necessary for developing wireless, passive, fully integrated, telemetric sensors for use in NDE applications. Efforts are currently underway to continue the research and development of our novel approach to realizing such a technology.

19

5. References

1. Toonen, R. C.; Fu, R. X.; Ivill, M. P.; Hirsch, S. G.; Cole, M. W.; Zheleva, T. S. *A Fully Integrated Materials Framework for Enabling the Wireless Detection of Micro-defects in Aging and Battle-worn Structures*; ARL-MR-0775; U.S. Army Research Laboratory: Aberdeen Proving Ground, MD, April 2011.

2. Morito, K.; Iwazaki, Y.; Suzuki, T.; Fujimoto, M. *J. Appl. Phys.* **2003**, *94*, 5199.

3. Gevorgian, S.; Vorobiev, A.; Lewin, T. *J. Appl. Phys.* **2006**, *99*, 124112.

4. Tappe, S.; Böttger, U.; Waser, R. *Appl. Phys. Lett.* **2004**, *85*, 624.

5. Noeth, A.; Yamada, T.; Sherman, V. O.; Muralt, P.; Tagantsev, A. K.; Setter, N. *J. Appl. Phys.* **2007**, *102*, 114110.

6. Cole, M. W.; Geyer, R. G. *Mechanics of Materials* **2004**, *36*, 1017.

7. Cole, M. W.; Toonen, R. C.; Ivill, M.; Hirsch, S. G.; Ngo, E.; Hubbard, C. *J. Appl. Phys.* **2011**, *110*, 124105.

8. Nishiyama, H.; Nakamura, M. *IEEE Trans. Comp., Hybrids, Manuf. Technol.* **1993**, *16*, 360.

9. Bevington, P. R.; Robinson, D. K. *Data Reduction and Error Analysis for the Physical Sciences*, McGraw-Hill, New York, 43–48, 1992.

10. Barker, A. S.; Hopfield, J. J. *Phys. Rev.* **1964**, *135*, A1732.

11. von Hippel, A. R. *Dielectrics and Waves*; Wiley, New York, 1954, pp. 102, 161.

12. York, B. "Tunable dielectrics for RF circuits," in *Multifunctional Adaptive Microwave Circuits and Systems*, M. Steer, Ed. Raleigh, NC:Scitech, 2009.

13. Basceri, C.; Streiffer, S. K.; Kingon, A. I.; Waser, R. *J. Appl. Phys.* **1997**, *82*, 2497.

14. Pertsev, N. A;. Zembilgotov, A. G.; Tagantsev, A. K. *Phys. Rev. Lett.* **1998**, *80*, 1988.

15. Zhang, J.; Heitmann, A. A.; Alpay, S .P.; Rossetti, G. A., Jr. *J. Mater. Sci.* **2009**, *44*, 5263.

16. Chase, D.; Chen, L.-Y.; York, R. *IEEE Trans. Microwave Theory Tech.* **2005**, *53*, 3215.

17. Damjanovic, D. *Rep. Prog. Phys.* **61**, 1267, 1998.

18. Giurgiutiu, V.; Zagrai, A. N.; Bao, J. J. *Structural Health Monitoring* **2002**, *1*, 41–61.

19. Elburn, E.; Toonen, R. Acoustic Nondestructive Evaluation of Aircraft Paneling Using Piezoelectric Sensors, in preparation.

6. Transitions

This effort has resulted in journal paper, two conference papers, three ARL reports (including this document), and multiple conference presentations. Fabrication developments and measurement techniques have been successfully transitioned into the mission and customer programs of the Integrated Electromagnetic Materials Team.

6.1   Journal Papers

Toonen, Ryan C.; Cole, M. W. Third-Order Electric-Field-Induced Dipolar Resonances from Patterned Barium-Strontium-Titanate Thin-Films. Submitted to *Applied Physics Letters* on February 27, 2012; accepted May 2012.

6.2   Conference Papers

Fu, R. X.; Toonen, R. C.; Ngo, E. H.; Cole, M. W.; Hirsch, S. G.; Ivill, M. P.; Hubbard, C.W. Pb(Zr,Ti)O3 (PZT) Thin Film Sensors for Fully-Integrated, Passive Telemetric Transponders. *Sensors & Transducers J.* **2011**, *11*, 34.

Toonen, R. C.; Ngo, E. H.; Cole, M. W.; Hirsch, S. G.; Ivill, M. P.; Hubbard, C. W.; Fu, R. X. Tunable Split-Ring Resonator Devices for Compact, Frequency-Selective, Back-Scatter Transponders, *27th Army Science Conf. Proc.* NP-12, December 2010.

6.3   ARL Reports

Toonen, R. C.; Fu, R. X.; Ivill, M. P.; Hirsch, S. G.; Cole, M. W.; Zheleva, T. S. *A Fully Integrated Materials Framework for Enabling the Wireless Detection of Micro-defects in Aging and Battle-worn Structures*; ARL-MR-0775; U.S. Army Research Laboratory: Aberdeen Proving Ground, MD, April 2011.

Elburn, E.; Toonen, R. *Acoustic Nondestructive Evaluation of Aircraft Paneling Using Piezoelectric Sensors*; in preparation.

6.4   Oral Presentations

Fu, R. X.; Toonen, R. C.; Ivill, M. P.; Hirsch, S. G.; Brown, N.; Cole, M. W. Fully-Integrated, Thin-Film Piezoelectric Sensors for Wireless, Non-Destructive Evaluation of Aging Structures, 20th IEEE International Symposium on Applications of Ferroelectrics / International Symposium on Piezoresponse Force Microscopy & Nanoscale Phenomena in Polar Materials (ISAF-2011-PFM) Joint Conference, Vancouver, Canada, July 24-27, 2011,.

Brown, N.; Toonen, R. C.; Archibald, W.; Cole, M. W. The Speed of Sound Through PZT. Twelfth Annual Fall Research Symposium, College of Science & Mathematics, University of the Virgin Islands, St. Thomas Campus, Fall Semester 2010.

6.5 Poster Presentations

Fu, R. X.; Toonen, R. C.; Ivill, M. P.; Ngo, E. H.; Cole, M. W.; Hirsch, S. G.; Hubbard, C. W Integrated Piezoelectric and Ferroelectric Thin Films for Passive Telemetric Transponders, 20th IEEE International Symposium on Applications of Ferroelectrics / International Symposium on Piezoresponse Force Microscopy & Nanoscale Phenomena in Polar Materials (ISAF-2011-PFM) Joint Conference, Vancouver, Canada July 24–27, 2011.

Toonen, R. C.; Ngo, E. H.; Cole, M. W.; Hirsch, S. G.; ; Ivill, M. P.; Hubbard, C. W. A Fully-Integrated Materials Framework for Enabling the Wireless Detection of Micro-Defects in Aging and Battle-Worn Structures, 27th Army Science Conference; JW Marriott, November 29 – December 2, 2010, Orlando, FL.

Archibald, W.; Brown, N.; Toonen, R. C.; Cole, M. W. Structural Health Monitoring System for Military Vehicles and Aircrafts, 2010 Materials Research Society Fall Meeting & Exhibit, Boston, MA, November 29–December 3, 2010.

List of Symbol, Abbreviations, and Acronyms

Al	aluminum
Al_2O_3	sapphire
ARL	U.S. Army Research Laboratory
BOE	buffered oxide etchant
$BaTiO_3$	barium titanate
BST	barium strontium titanate
BW	bandwidth
CFA	conventional furnace annealing
C-V	capacitance-voltage
DAQ	data acquisition unit
DoD	Department of Defense
DRI	Director's Research Initiative
DSP	digital signal processing
DUT	device under test
EM	electromagnetic
FPGA	field-programmable gate array
GWU	George Washington University
HF	hydrofluoric acid
TEM	transmission electron microscope
I	In-Phase
IC	integrated circuit
IDC	inter-digital finger capacitor
ISM	industrial, scientific, and medical
LDG	Landau-Devonshire-Ginzberg

MIM	metal-insulator-metal
MOSD	metal organic solution deposition
MW	microwave
NDE	nondestructive evaluation
NH_4F	ammonium fluoride
NiCr	nickel chromium alloy
PM	phase modulation
Pt	platinum
PWASs	piezoelectric wafer active sensors
PZT	lead zirconate titanate
Q	Quadrature
RBS	Rutherford backscattering spectrometry
RFID	radio frequency identification
RMS	root mean square
RTA	rapid thermal annealer
SEAP	Science & Engineering Apprentice Program
Si	silicon
SOL	short-open-load
$SrTiO_3$	strontium titanate
TX/RX	transmitting/receiving
UD	ultrasonic detector
UV	ultraviolet
VCO	voltage controlled oscillator
XDCR	piezoelectric transducer

No. of
Copies   Organization

4 HCS   US ARMY RSRCH LAB
          ATTN RDRL WMM E
           R C TOONEN
           M P IVILL
           S GARY HIRSCH,
           M W COLE
          BLDG 4600
          ABERDEEN PROVING GROUND MD
          21005-5066

 4 HCS   US ARMY RSRCH LAB
          ATTN RDRL SEE E R FU
          ATTN RDRL SEE G WOOD
          ATTN RDRL SEE E K ALIBERTI
          ATTN RDRL SED E T ZHELEVA
          2800 POWDER MILL ROAD
          ADELPHI MD 20783-1197

TOTAL: 8 HCS

INTENTIONALLY LEFT BLANK.